

Low-Loss All-Optical Zeno Switch in a Microdisk Cavity Using EIT

B. D. Clader,^{1,*} S. M. Hendrickson,¹ R. M. Camacho,² and B. C. Jacobs¹

¹*The Johns Hopkins University Applied Physics Laboratory, Laurel, MD, USA*

²*Sandia National Laboratories, Albuquerque, NM, USA*

We present theoretical results of a low-loss all-optical switch based on electromagnetically induced transparency and the classical Zeno effect in a microdisk resonator. We show that a control beam can modify the atomic absorption of the evanescent field which suppresses the cavity field buildup and alters the path of a weak signal beam. We predict more than 35 dB of switching contrast with less than 0.1 dB loss using just 2 μW of control-beam power for signal beams with less than single photon intensities inside the cavity.

I. INTRODUCTION

Over the past few decades transistors and other computing components have dropped in size while simultaneously increasing performance. However, power dissipation is increasingly becoming a fundamental limitation to performance [1]. All-optical switches and transistors seek to address this issue, while simultaneously pushing forward the technology needed to create all-optical quantum computing devices [2–6]. One of the fundamental issues limiting this technology is the strength of the nonlinear effects that couple the signal and control fields. Electromagnetically induced transparency (EIT) [7, 8] has been investigated as a resource for optical switches [9–12] and quantum memories [13–16] due to its large nonlinearity, which is enhanced by coherent effects. We demonstrate how it can be used along with a microdisk resonator to create a high-speed low-loss all-optical switch.

The quantum Zeno effect (QZE) [17] is a process whereby frequent measurements of a quantum system can inhibit transitions. In the first experimental demonstration, the QZE was shown to inhibit driven transitions between $^9\text{Be}^+$ ground-state hyperfine levels [18]. It has been demonstrated that a classical analogue to the QZE can be used to create an all-optical switch using two-photon absorption (TPA) in a resonant optical cavity [19, 20]. This switch consists of a four-port resonator evanescently coupled to Rubidium (Rb) vapor. The presence of two input beams results in sufficiently strong TPA to suppress the cavity field build-up thereby altering the path of the beams due to interference effects. All-optical Zeno switches have also been proposed using other nonlinearities including Raman [21] and inverse Raman induced loss [22].

In addition to classical switching applications, it was shown that the Zeno effect could be used for quantum information purposes. With a sufficiently strong nonlinearity, it could enable quantum logic gates [23, 24] without the need for a large number of ancilla photons. The ability of the QZE to inhibit transitions could be used instead of protective ancilla photons to ensure that error

events are suppressed in photonic quantum gates [25–29]. Related work has studied the QZE as a tool for protecting entanglement [30] and its effect on entanglement [31] in general. It has also been suggested that the QZE could be used to implement quantum logic gates using semiconductor materials [32].

Here we report theoretical results and performance estimates showing that EIT and Autler–Townes splitting [33] can also be used to implement an all-optical switch in a microdisk cavity based on the Zeno effect. We make use of single photon absorption (SPA) to suppress the resonant field buildup in a cavity, and use a control beam to modulate the absorption by inducing EIT (we refer to the combined EIT and Autler–Townes splitting effect as simply EIT from here out). The benefit of this approach is that on-resonant SPA has a higher absorption cross-section than known nonlinear processes, potentially enabling better switching results as long as SPA can be sufficiently reduced by EIT. In addition this approach allows the use of very weak signal beams, making it a good candidate to switch single-photon intensities with low loss.

To understand how the switch operates, consider the operation of a four-port resonator, as shown in Fig. 1, in the absence of any atomic interaction (see e.g. [34] and [35] for detailed discussions of four-port resonators and nomenclature). On resonance, a weakly-coupled signal E_{in} will be almost completely transferred to the drop-port as a result of destructive interference between the resonant build-up of the cavity field and the light in the input waveguide. Next, consider how this system would change with the addition of a strong loss mechanism in the cavity, such as shown in Fig. 1(a). The resonant field buildup of the signal beam will be suppressed which dramatically reduces the destructive interference in the input waveguide and results in nearly all of the incident light exiting the through-port. Counter-intuitively, the presence of the strong loss mechanism will not dramatically increase the loss of the system but will instead alter the coupling condition of the cavity which changes the output path of the light.

This is directly analogous to the suppression of probability amplitudes via measurement in the quantum Zeno effect. This is made more clear when considering the case of single photons in the signal beam. In that case, a null

* dave.clader@jhuapl.edu

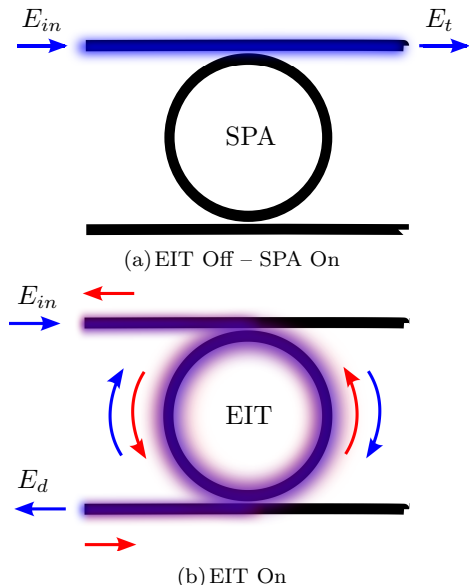


Figure 1. Schematic of the EIT based Zeno all-optical micro-resonator switch.

(a) When only a single input beam is weakly coupled to the cavity, strong SPA inhibits field buildup causing the beam to bypass the resonator and exit via the through port E_t .

(b) When two beams are present, denoted by blue for the signal beam and red for the control beam, the control beam eliminates the evanescent coupling of the fields to the atoms surrounding the cavity through EIT. This reduces the loss present, allowing the signal beam to build in the resonator, exiting through the drop port E_d .

absorption (measurement) event by the atoms surrounding the cavity causes the photon to bypass the resonator. The stronger this potential absorption process, the more likely that a null absorption event occurs and the photon bypasses the cavity. More information on this can be found in Refs. [19, 26].

Now we consider a loss mechanism based on a cascade EIT scheme using the $5S_{1/2}$, $5P_{3/2}$ and $5D_{5/2}$ states of Rb. We take the signal beam to be resonant with the $5S_{1/2} \rightarrow 5P_{3/2}$ transition near 780 nm and the control beam to be resonant with the $5P_{3/2} \rightarrow 5D_{5/2}$ transition near 776 nm. When the 776 nm EIT control beam is present, a transmission window is created in the 780 nm single-photon absorption line. This allows the signal beam to build in the resonator and exit through the drop port, as shown schematically in Fig. 1(b).

In this paper, we theoretically analyze the performance of such a device using high-fidelity numerical models and present detailed estimates of switching performance. Our results indicate that this scheme enables high-contrast, low-loss switching at timescales on the order of the total cavity relaxation time which is roughly ~ 100 picoseconds for the devices under consideration in this paper.

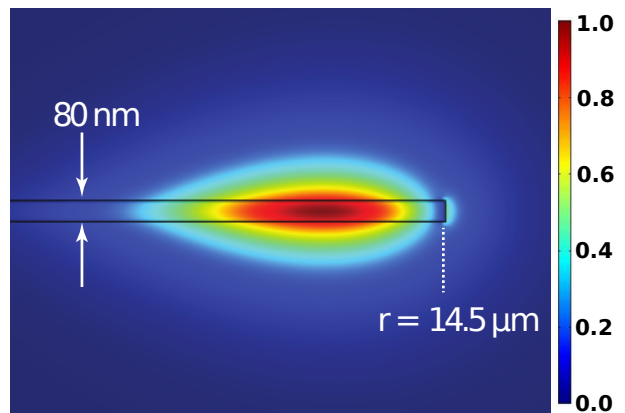


Figure 2. Simulated normalized electric field profile of the microdisk, showing the radial component of the mode used in the quantum calculation. The cutout is the along page (side) view of Fig. 1. The radius of the device is set such that the free spectral range is equal to 4 nm, allowing for simultaneous resonance at 780nm and 776nm, and the thickness of the disk is chosen such that 30% of the field is outside the resonator.

II. THEORETICAL MODEL

We model the transmission characteristics of the four-port microdisk shown in Fig. 1 evanescently coupled to Rubidium vapor. The device specifications have been chosen to be consistent with current fabrication capabilities. The design consists of an unclad, suspended Si_3N_4 disk with a free spectral range equal to the 4 nm difference between the $5S_{1/2} \rightarrow 5P_{3/2}$ D_2 line at 780 nm and the $5P_{3/2} \rightarrow 5D_{5/2}$ line at 776 nm, allowing for simultaneous resonance at 776 nm and 780 nm (for an example of a similar device operating at a higher wavelength see Ref. [20]). The thickness is chosen such that roughly 30% of the electric field energy of the fundamental mode is outside the resonator, allowing considerable interaction with the Rubidium vapor surrounding the cavity.

We estimate the field profile of the fundamental mode in the cavity using a fully vectorial 2-D axially symmetric weighted residual formulation of Maxwell's equations implemented in Comsol Multiphysics software (as shown in Fig. 2). The field profile is used to estimate the evanescent interaction of signal and control beams with an ensemble of three-level atoms by calculating the effective absorption coefficient. This calculated absorption coefficient is combined with a classical model of a resonator to predict switching performance. The intent is to show that the presence of the control beam will induce EIT, modifying the absorption coefficient of the signal beam in the resonator. This causes a change in the overall coupling between the waveguide and the resonator resulting in switching.

A. Atomic Model

The device under consideration is designed to support simultaneous cavity resonances at the 780 nm and 776 nm spectral lines of Rubidium. To model this interaction between the cavity fields and the Rubidium vapor, we approximate the Rubidium atom as the four-level atomic system shown in Fig. 3. The fourth level, indicated on the right, is the decay channel from the excited state level $|3\rangle$ to the ground state level $|1\rangle$ through the $6P_{3/2}$ level. It is included in our atomic model only as a decay term. The Hamiltonian of this system is the standard three-level cascade model given by

$$H = \left(-\hbar\frac{\Omega_s}{2}|1\rangle\langle 2| - \hbar\frac{\Omega_c}{2}|2\rangle\langle 3| + \text{h.c.} \right) \quad (1)$$

$$+ \hbar\Delta_s|1\rangle\langle 1| - \hbar\Delta_c|3\rangle\langle 3|.$$

We denote all variables associated with the 776 nm control field and 780 nm signal field with the subscripts c and s respectively. The Rabi frequency is $\Omega = 2\vec{d} \cdot \hat{\epsilon}\mathcal{E}/\hbar$, where \vec{d} is the dipole moment, \mathcal{E} is the slowly varying electric field amplitude, $\hat{\epsilon}$ is the polarization vector, and Δ is the detuning of the field from its associated transition. This Hamiltonian, along with the addition of phenomenological decay terms, gives the following density matrix equations:

$$\dot{\rho}_{11} = i\frac{\Omega_s}{2}\rho_{21} - i\frac{\Omega_s^*}{2}\rho_{12} + \Gamma_{12}\rho_{22} + \Gamma_{13}\rho_{33} \quad (2a)$$

$$\dot{\rho}_{22} = i\frac{\Omega_c}{2}\rho_{32} - i\frac{\Omega_c^*}{2}\rho_{23} + i\frac{\Omega_s^*}{2}\rho_{12} - i\frac{\Omega_s}{2}\rho_{21} \quad (2b)$$

$$- \Gamma_{12}\rho_{22} + \Gamma_{23}\rho_{33}$$

$$\dot{\rho}_{33} = i\frac{\Omega_c^*}{2}\rho_{23} - i\frac{\Omega_c}{2}\rho_{32} - (\Gamma_{13} + \Gamma_{23})\rho_{33} \quad (2c)$$

$$\dot{\rho}_{12} = i\frac{\Omega_s}{2}(\rho_{22} - \rho_{11}) - i\frac{\Omega_c^*}{2}\rho_{13} - i(\Delta_s - i\gamma_{12})\rho_{12} \quad (2d)$$

$$\dot{\rho}_{13} = i\frac{\Omega_s}{2}\rho_{23} - i\frac{\Omega_c}{2}\rho_{12} - i(\Delta_s + \Delta_c - i\gamma_{13})\rho_{13} \quad (2e)$$

$$\dot{\rho}_{23} = i\frac{\Omega_c}{2}(\rho_{33} - \rho_{22}) - i\frac{\Omega_c}{2}\rho_{22} - i(\Delta_c - i\gamma_{23})\rho_{23}, \quad (2f)$$

where Γ_{mn} is the homogeneous decay term associated with the $m \rightarrow n$ transition, and γ_{mn} is the transverse decay term associated with the off-diagonal elements. We take $\gamma_{12} = \Gamma_{12}/2$, $\gamma_{13} = (\Gamma_{13} + \Gamma_{23})/2$, and $\gamma_{23} = (\Gamma_{12} + \Gamma_{13} + \Gamma_{23})/2$. These off-diagonal decay rates assume that all decoherence is due to population decay, which is suitable for atomic vapors. The values were chosen to be physically consistent with a positive density matrix, which does not always hold for arbitrary decoherence terms [36, 37]. The branching ratio between the Γ_{23} and Γ_{13} decay channels was set to 0.65 : 0.35 as given in Ref. [38].

Many analytic solutions to Eqs. (2) and similar models have been analyzed [8, 39–41]. However, to ensure accurate device performance estimates, we use numerical solu-

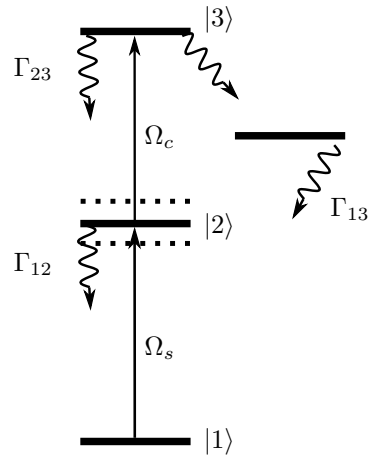


Figure 3. The three-level atom we use to model the resonant $5S_{1/2} \rightarrow 5P_{3/2}$ and $5P_{3/2} \rightarrow 5D_{5/2}$ transitions in Rubidium, including all decay channels. The dotted lines indicate the $5P_{3/2}$ splitting induced by the upper beam. The state on the right is the $6P_{3/2}$ which provides a decay channel from the $5D_{5/2}$ excited state to the $5S_{1/2}$ ground state.

tions to the density matrix equations above. This allows us to solve Eqs. (2), with only a steady-state approximation, which is consistent with our experiments using CW lasers. However we do not make any perturbation approximations since we assume a high-Q resonator, which can develop intense fields. The steady-state approximation can easily be lifted to model pulsed phenomena, however we include it here in order to reduce the run-time of our numerical simulations.

We include Doppler broadening in our simulations to account for thermal motion of the atoms. We do so by averaging the density matrix elements over the Doppler profile given by

$$F(\Delta) = \frac{1}{\sqrt{2\pi}\sigma_D} e^{-\frac{\Delta^2}{2\sigma_D^2}}, \quad (3)$$

where Δ is the laser field detuning due to the thermal velocity of the atom, and σ_D is the Doppler linewidth, given by the Maxwell-Boltzmann velocity distribution.

B. Cavity – Waveguide Coupling Model

We model the coupling of the waveguides to the cavity using the coupled-mode equations of Haus [34] (see also [35]). This method is related to the E&M approach taken in [19], and we get nearly identical results using either technique. We will label the ports as done in Fig. 1. The input port will be called “in” and corresponds to the upper left waveguide in the figures, and the two output ports will be labelled the “drop” port and “through” port for the lower left and upper right waveguides respectively.

The equation governing the field amplitude inside the

resonator for a single input field is given by

$$\frac{da}{dt} = -i\Delta a - \frac{1}{2}(\kappa_0 + \kappa_e + \kappa_1 + \kappa_2)a + i\sqrt{\kappa_1}s_{in}, \quad (4)$$

where a is the field amplitude inside the resonator, $\Delta = (\omega - \omega_0)$ is the detuning of the field with frequency ω from the cavity resonance of frequency ω_0 , κ_0 is the intrinsic cavity linewidth, κ_e is related to the absorption rate of the atoms, κ_1 and κ_2 are the cavity – waveguide coupling rates for waveguides 1 and 2 respectively, and $|s_{in}|^2$ is the input power.

The steady state solution to Eq. (4) is

$$a = i \frac{2\sqrt{\kappa_1}}{2i\Delta + (\kappa_0 + \kappa_e + \kappa_1 + \kappa_2)} s_{in}. \quad (5)$$

The power out the through port is related to the power in plus the component that couples out from the resonator

$$s_t = s_{in} + i\sqrt{\kappa_1}a = \frac{2i\Delta + (\kappa_0 + \kappa_e - \kappa_1 + \kappa_2)}{2i\Delta + (\kappa_0 + \kappa_e + \kappa_1 + \kappa_2)} s_{in}. \quad (6)$$

The signal power out the drop port is related to the power that couples out from the resonator,

$$s_d = i\sqrt{\kappa_2}a = \frac{-2\sqrt{\kappa_1\kappa_2}}{2i\Delta + (\kappa_0 + \kappa_e + \kappa_1 + \kappa_2)} s_{in}. \quad (7)$$

The through port and drop port transmission rates can now be easily calculated. They are simply $T = |s_t|^2/|s_{in}|^2$ and $D = |s_d|^2/|s_{in}|^2$ which yield

$$T = \frac{4\Delta^2 + (\kappa_0 + \kappa_e - \kappa_1 + \kappa_2)^2}{4\Delta^2 + (\kappa_0 + \kappa_e + \kappa_1 + \kappa_2)^2} \quad (8a)$$

$$D = \frac{4\kappa_1\kappa_2}{4\Delta^2 + (\kappa_0 + \kappa_e + \kappa_1 + \kappa_2)^2}. \quad (8b)$$

The intrinsic quality factor is defined as $Q_0 = \omega_0/\kappa_0$ and the external quality factor is $Q_{ext} = \omega_0/(\kappa_e + \kappa_1 + \kappa_2)$. By controlling the atomic absorption rate κ_e we can modify the external Q of the atom-resonator system causing the coupling conditions to change, resulting in the ability to switch between the drop port and through port.

C. Cavity Field – Atomic Interaction Model

The interaction of the evanescent fields to the Rubidium surrounding the cavity is the source of the added loss κ_e in the waveguide–resonator coupling model above. To give performance estimates for the switch, we calculate the average absorption coefficient of the signal beam in the resonator.

To calculate κ_e we first solve the atomic equations, including Doppler broadening, given in (2) for a particular value of the signal and control beam fields. The base absorption coefficient from standard quantum-optics theory

is given by:

$$\alpha(\Omega_s, \Omega_c) = \frac{4Nd^2\omega\chi_{12}(\Omega_s, \Omega_c)}{\hbar\epsilon_0c}, \quad (9)$$

where $\chi_{12}(\Omega_s, \Omega_c) = \text{Im}[\rho_{12}(\Omega_s, \Omega_c)]/\Omega_s$ is related to the linear susceptibility and is dependent upon: signal and control beam Rabi frequencies, the density N of Rubidium atoms, the dipole moment d and the angular frequency ω of the 780 nm transition. Here we explicitly note the functional dependence of all terms that depend upon the Rabi frequencies (field amplitudes) for clarity.

The small mode volume and high Q of the microdisk produce large intra-cavity intensities for even modest input power levels. This can induce large splitting of the intermediate level. However, the field distribution of the control beam outside the resonator falls off sharply as shown in Fig. 2. To capture this, we compute the density matrix elements for each Rabi frequency corresponding to the different field values, and then average over the field distributions of both the signal and control fields as shown in Eq. (10) below. These solutions are then averaged and weighted by the normalized signal beam intensity, to give the average absorption coefficient for the signal beam. This average absorption coefficient $\bar{\alpha}$ is given by

$$\bar{\alpha} = \int_{V_e} \alpha(\Omega_s, \Omega_b)w(\vec{r})dV, \quad (10)$$

where the integral is taken to extend over the volume external to the resonator, denoted by V_e , and the weighting function

$$w(\vec{r}) = \frac{|\Omega_s(\vec{r})|^2}{\int_{V_t} |\Omega_s(\vec{r})|^2 dV} \quad (11)$$

scales with the signal beam intensity.

The normalization integral in the denominator of the weighting function extends over the entire volume of integration V_t , including the region interior to the resonator, as opposed to the integral in Eq. (10) which is only over the region exterior to the resonator. This accounts for the fact that the field inside the resonator does not interact with the Rubidium thus reducing the overall strength of the interaction. This weighting also accounts for the fact that the scattering cross section is larger near regions of high signal beam intensity than regions of low intensity. We assume that both beams are contained in the same cavity mode for this calculation.

We can relate the average absorption coefficient, $\bar{\alpha}$ to the external cavity loss rate κ_e through the simple relation $\kappa_e = c\bar{\alpha}$, where c is the speed of light in the cavity. Thus, by changing the atomic absorption coefficient $\bar{\alpha}$ through EIT, we can modify the total cavity Q, resulting in changing coupling conditions and switching.

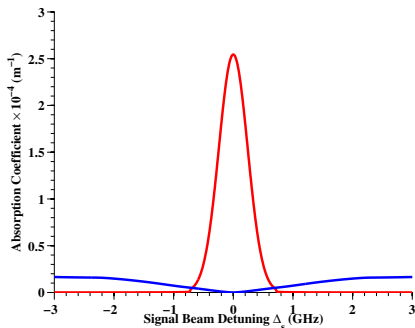


Figure 4. Average absorption coefficient, denoted by $\bar{\alpha}$ in the text, of the signal beam with the control beam on (blue curve) and control beam off (red curve), plotted as a function of the signal beam detuning, Δ_s . With the control beam on, the standard Doppler broadened line is split. Because of the non-uniform control field intensity, the usual Autler–Townes splitting is replaced with the absorption profile shown in blue.

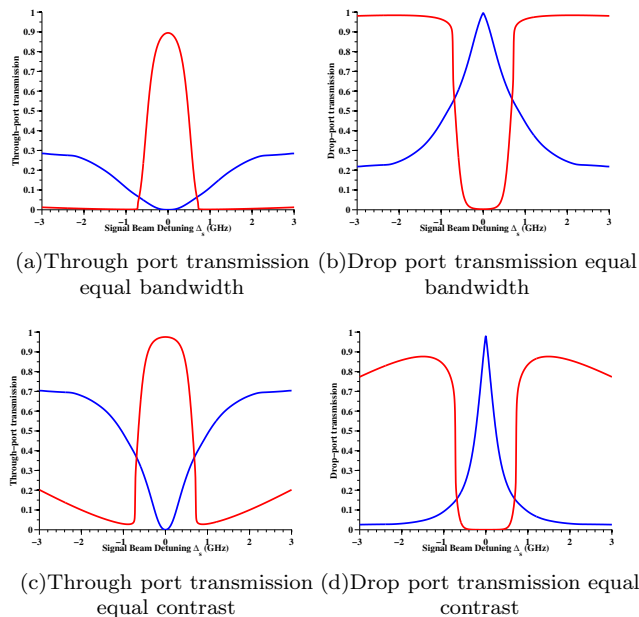


Figure 5. Through and drop port transmission plots for the parameters given in Tables II and III. Each plot provides the transmission percentage as a function of the signal laser detuning from the cavity resonance. The red curve corresponds to the case where EIT is off, and the blue curve corresponds to the case when the EIT control beam is on. In figures (a) and (b) we use the parameters in Table II to equalize the bandwidth in both ports. In figures (c) and (d) we use the parameters in Table III where the coupling condition was chosen such that the contrast was equalized.

III. RESULTS

Using the methodology above, the average absorption coefficient of the signal beam is calculated and plotted in Fig. 4, with the control beam on and off (blue and red

Table I. Parameters used in atomic simulation.

Variable	Description	Value	Units
P_c	Control Beam Power	2.0	μW
P_s	Signal Beam Power	20	fW
A_m	Effective Mode Area	8.2×10^{-10}	cm^2
N	Rubidium Density	5.0×10^{12}	cm^{-3}
d_s	Lower dipole moment	2.1×10^{-29}	$\text{m}\cdot\text{C}$
d_c	Upper dipole moment	4.6×10^{-30}	$\text{m}\cdot\text{C}$
Γ_{12}	Lower decay rate	6.0	MHz
Γ_{23}	Upper decay rate	280	kHz
Γ_{13}	Upper decay rate	150	kHz
σ_D	Doppler linewidth	240	MHz

curves respectively). All relevant atomic parameters for this simulation are given in Table I. The spectral shape of the absorption coefficient is modified from the typical double-Lorentzian peaks associated with Autler–Townes splitting because of Doppler broadening and the transverse variation of control beam intensity in the evanescent field. This causes the signal beam to see a distribution of EIT windows rather than a single split line as would be the case in a uniform field. Very large Autler–Townes splitting on the order of GHz is possible, because the high-Q and small mode volume of the resonator can generate high-intensity fields with relatively modest input powers.

Upon calculating the average absorption coefficient of the signal beam in the resonator, we estimate the transmission of the through-port (Fig. 5(a)) and drop-port (Fig. 5(b)) with and without the control beam, using the formulas in Eq. (8). We take the waveguides to be strongly over-coupled to the cavity with κ_1 and κ_2 roughly two orders of magnitude larger than κ_0 . The coupling rates were chosen to equalize the bandwidth on the through-port and drop-port. With this constraint, we estimate the on-resonant switching contrast to be 50 dB in the through-port and 25 dB in the drop-port, along with only 0.5 dB and 0.02 dB of loss in each respectively. We define the bandwidth as the point at which the switching contrast reaches 20 dB, on Figs. 5(a) and 5(b). This gives a bandwidth of approximately 516 MHz for each output port. These results are tabulated in Table II.

Switching performance trade-offs can be analyzed by varying the coupling rates between the waveguides and cavity. In the previous example, we chose to equalize the bandwidth in the through-port and drop-port. This required strongly over-coupling the waveguides to the cavity. We can instead choose to equalize the contrast, and by extension the loss in each port. To do this, we lower the fixed waveguide–cavity coupling rates which could be done by increasing the distance between the waveguides and the cavity for example. These results are shown in Figs. 5(c) and 5(d), with the corresponding performance metrics given in Table III. On cavity resonance we esti-

Table II. Switch performance results - equal bandwidth

Variable	Description	Value	Units
Q_0	Intrinsic Quality Factor	3.6×10^6	-
κ_1	Waveguide 1 coupling	26.7	GHz
κ_2	Waveguide 2 coupling	26.7	GHz
Results			
	Through port loss	0.5	dB
	Through port contrast	50	dB
	Drop port loss	0.02	dB
	Drop port contrast	25	dB
	Through port bandwidth	500	MHz
	Drop port bandwidth	500	MHz

mate 38 dB switching contrast with only 0.1 dB loss in each port. The tradeoff for equalized contrast, and lower loss is a reduced bandwidth in the through-port of 330 MHz, however the drop-port bandwidth is increased a comparable amount due to conservation of energy constraints.

IV. CONCLUSIONS

We have presented numerical simulations demonstrating the effectiveness of using EIT together with the classical Zeno effect to create an all-optical switch in a micro-

resonator. Because of the large resonant build-up that the micro-resonators allow, even with modest input powers, very high intensity control fields can be created which can create excellent switching contrast with low loss. In addition, this method is compatible with a very low input power signal. These properties suggest that such a device could be suitable for switching single-photon intensities, ideal for some quantum information applications.

Table III. Switch performance results - equal contrast

Variable	Description	Value	Units
Q_0	Intrinsic Quality Factor	3.6×10^6	-
κ_1	Waveguide 1 coupling	5.9	GHz
κ_2	Waveguide 2 coupling	5.9	GHz
Results			
	Through port loss	0.1	dB
	Through port contrast	38	dB
	Drop port loss	0.1	dB
	Drop port contrast	38	dB
	Through port bandwidth	170	MHz
	Drop port bandwidth	840	MHz

ACKNOWLEDGMENTS

Funding was provided in part by IRAD and the DARPA ZOE program (Contract No. W31P4Q-09-C-0566). We acknowledge thought provoking discussions with Jim Franson and Todd Pittman.

-
- [1] N. Kim, T. Austin, D. Baauw, T. Mudge, K. Flautner, J. Hu, M. Irwin, M. Kandemir, and V. Narayanan, *Computer*, **36**, 68 (2003).
 - [2] D. Miller, *Nature Photonics*, **4**, 3 (2010).
 - [3] A. M. C. Dawes, L. Illing, S. M. Clark, and D. J. Gauthier, *Science*, **308**, 672 (2005).
 - [4] X. Hu, P. Jiang, C. Ding, H. Yang, and Q. Gong, *Nature Photonics*, **2**, 185 (2008).
 - [5] M. Waldow, T. Plötzing, M. Gottheil, M. Först, J. Bolten, T. Wahlbrink, and H. Kurz, *Opt. Express*, **16**, 7693 (2008).
 - [6] M. Albert, A. Dantan, and M. Drewsen, *Nature Photonics*, **5**, 633 (2011).
 - [7] S. E. Harris, *Physics Today*, **50**, 36 (1997).
 - [8] M. Fleischhauer, A. Imamoglu, and J. P. Marangos, *Rev. Mod. Phys.*, **77**, 633 (2005).
 - [9] M. Bajcsy, S. Hofferberth, V. Balic, T. Peyronel, M. Hafezi, A. S. Zibrov, V. Vuletic, and M. D. Lukin, *Phys. Rev. Lett.*, **102**, 203902 (2009).
 - [10] J. Zhang, G. Hernandez, and Y. Zhu, *Opt. Lett.*, **32**, 1317 (2007).
 - [11] M. Fleischhauer, *Science*, **333**, 1228 (2011).
 - [12] A. K. Popov, S. A. Myslivets, and T. F. George, *Phys. Rev. A*, **71**, 043811 (2005).
 - [13] D. F. Phillips, A. Fleischhauer, A. Mair, R. L. Walsworth, and M. D. Lukin, *Phys. Rev. Lett.*, **86**, 783 (2001).
 - [14] A. V. Turukhin, V. S. Sudarshanam, M. S. Shahriar, J. A. Musser, B. S. Ham, and P. R. Hemmer, *Phys. Rev. Lett.*, **88**, 023602 (2001).
 - [15] A. Mair, J. Hager, D. F. Phillips, R. L. Walsworth, and M. D. Lukin, *Phys. Rev. A*, **65**, 031802 (2002).
 - [16] M. D. Lukin, *Rev. Mod. Phys.*, **75**, 457 (2003).
 - [17] B. Misra and E. Sudarshan, *J. of Math. Phys.*, **18**, 756 (1977).
 - [18] W. M. Itano, D. J. Heinzen, J. J. Bollinger, and D. J. Wineland, *Phys. Rev. A*, **41**, 2295 (1990).
 - [19] B. C. Jacobs and J. D. Franson, *Phys. Rev. A*, **79**, 063830 (2009).
 - [20] S. M. Hendrickson, C. N. Weiler, R. M. Camacho, P. T. Rakich, A. I. Young, M. J. Shaw, T. B. Pittman, J. D. Franson, and B. C. Jacobs, arXiv:1206.0930v1 (2012).
 - [21] Y. H. Wen, O. Kuzucu, T. Hou, M. Lipson, and A. L. Gaeta, *Opt. Lett.*, **36**, 1413 (2011).
 - [22] K. Kieu, L. Schneebeli, E. Merzlyak, J. M. Hales, A. DeSimone, J. W. Perry, R. A. Norwood, and N. Peyghambarian, *Opt. Lett.*, **37**, 942 (2012).

- [23] E. Knill, R. Laflamme, G. Milburn, *et al.*, *Nature*, **409**, 46 (2001).
- [24] P. Kok, W. J. Munro, K. Nemoto, T. C. Ralph, J. P. Dowling, and G. J. Milburn, *Rev. Mod. Phys.*, **79**, 135 (2007).
- [25] A. Beige, D. Braun, B. Tregenna, and P. L. Knight, *Phys. Rev. Lett.*, **85**, 1762 (2000).
- [26] J. D. Franson, B. C. Jacobs, and T. B. Pittman, *Phys. Rev. A*, **70**, 062302 (2004).
- [27] J. D. Franson, T. B. Pittman, and B. C. Jacobs, *J. Opt. Soc. Am. B*, **24**, 209 (2007).
- [28] Y. P. Huang and M. G. Moore, *Phys. Rev. A*, **77**, 062332 (2008).
- [29] X.-Q. Shao, H.-F. Wang, L. Chen, S. Zhang, Y.-F. Zhao, and K.-H. Yeon, *J. Opt. Soc. Am. B*, **26**, 2440 (2009).
- [30] S. Maniscalco, F. Francica, R. L. Zaffino, N. Lo Gullo, and F. Plastina, *Phys. Rev. Lett.*, **100**, 090503 (2008).
- [31] F. Francica, F. Plastina, and S. Maniscalco, *Phys. Rev. A*, **82**, 052118 (2010).
- [32] K. J. Xu, Y. P. Huang, M. G. Moore, and C. Piermarocchi, *Phys. Rev. Lett.*, **103**, 037401 (2009).
- [33] S. H. Autler and C. H. Townes, *Phys. Rev.*, **100**, 703 (1955).
- [34] H. A. Haus, *Wave and Fields in Optoelectronics* (Prentice-Hall, Englewood Cliffs, NJ, 1984) Chap. 7, pp. 197–234.
- [35] T. J. Kippenberg, S. M. Spillane, D. K. Armani, B. Min, L. Yang, and K. J. Vahala, “Fabrication, coupling and nonlinear optics of ultra-high-Q microcavities,” in *Optical Microcavities*, Advanced Series in Applied Physics, Vol. 5, edited by K. J. Vahala (World Scientific Publishing, Singapore, 2004) Chap. 5, pp. 177–238.
- [36] S. G. Schirmer and A. I. Solomon, *Phys. Rev. A*, **70**, 022107 (2004).
- [37] P. R. Berman and R. C. O’Connell, *Phys. Rev. A*, **71**, 022501 (2005).
- [38] O. S. Heavens, *J. Opt. Soc. Am.*, **51**, 1058 (1961).
- [39] T. Y. Popova, A. K. Popov, S. G. Rautian, and A. A. Feoktistov, *Soviet Physics JETP*, **30**, 243 (1970).
- [40] R. G. Brewer and E. L. Hahn, *Phys. Rev. A*, **11**, 1641 (1975).
- [41] J. Gea-Banacloche, Y.-q. Li, S.-z. Jin, and M. Xiao, *Phys. Rev. A*, **51**, 576 (1995).